

(Supplementary Information)

Field-free switching of perpendicular magnetization in an ultrathin epitaxial magnetic insulator

Sajid Husain^{†,‡,*}, Nicholas F. Prestes[†], Olivier Fayet[†], Sophie Collin[†], Florian Godel[†], Eric Jacquet[†], Thibaud Denneulin[‡], Rafal E. Dunin-Borkowski[‡], André Thiaville[§], Manuel Bibes[†], Henri Jaffrès[†], Nicolas Reyren^{†,*}, Albert Fert^{†,*}, and Jean-Marie George^{†,*}

[†]Laboratoire Albert Fert CNRS, Thales, Université Paris-Saclay, 1 avenue Augustin Fresnel-91767 Palaiseau Cedex

[‡]Ernst Ruska-Centre for Microscopy and Spectroscopy with Electrons, Forschungszentrum Jülich, 52425 Jülich, Germany.

[§]Laboratoire de Physique des Solides, Université Paris-Saclay, CNRS, 91405, Orsay, France.

^{||}Present address: Materials Sciences Division, Lawrence Berkeley National Laboratory, CA 94720, USA.

*Authors for correspondence

jeanmarie.george@cnsr-thales.fr

albert.fert@cnsr-thales.fr

nicolas.reyren@cnsr-thales.fr

shusain@lbl.gov

Table of Contents

I. Methods	2
II. TmIG thickness dependent X-ray diffraction	3
III. X-ray photoelectron spectroscopy (XPS)	3
IV. SQUID out-of-plane magnetization loop, magnetization at saturation.....	4
V. Resistivity	4
VI. Spin Hall magnetoresistance (SMR) and anomalous Hall effect (AHE).....	5
VII. Spin Hall magnetoresistance in different TmIG thickness	8
VIII. Harmonic Hall measurements: Spin orbit torques	9
IX. Dzyaloshinskii-Moriya Interaction (DMI) using Brillouin Light Scattering	11
X. Switching in TmIG(10)/Pt(6) in residual magnetic field (including earth magnetic field) only.....	13
XI. Zero-field switching in TmIG(7 nm)/Pt(6 nm) and TmIG(10 nm)/Pt(4 nm) bilayer devices	14
XII. Magnetization switching map in different devices of TmIG(10 nm)/Pt(6 nm)	15
XIII Kerr switching in 6-contact geometry device.	16
XV Magnetization switching in devices patterned at different angles.	17

I. Methods

Thin film growth: Thulium iron garnet ' $\text{Tm}_3\text{Fe}_5\text{O}_{12}$ (TmIG)' ferrimagnetic insulator (FIMI) thin films were deposited on (1 1 1) oriented $\text{Gd}_3\text{Ga}_5\text{O}_{12}$ (GGG) substrates by off-axis sputtering. Before deposition, substrates were treated by acetone and isopropyl alcohol in ultrasonication and subsequently annealed at 1000°C for 5 hours in a flow of pure oxygen (O_2) at atmospheric pressure. The substrates were transferred in air into the sputtering chamber for TmIG deposition. Thin films were deposited at room temperature in flow of Ar (40 sccm) and O_2 (20 sccm) with dynamic pressure 2.6×10^{-3} mbar (at 0.9 Pa nominal working pressure) with base pressure lower than $\sim 2 \times 10^{-8}$ mbar. Sample was rotated during growth at 5 rpm, The sputtering setup is composed by an ordinary MAK MEIVAC L200A01 cathode coupled to a SEREN R301 RF power source and a SEREN MC2 Matching BOX. The deposition rate was calibrated as 0.14 nm/minute at 40W of RF power using x-ray reflectivity. To promote crystallinity, these films were post-annealed (in *ex-situ* furnace) at 650°C for 4 hours in a flow of pure O_2 at atmospheric pressure. Further, a Pt layer of 6-nm thickness (unless otherwise stated) was deposited by on-axis magnetron sputtering at room temperature without further annealing. TmIG film surfaces were cleaned by O_2 plasma (~ 40 eV) before Pt deposition.

Structural characterization: X-Ray diffraction in symmetric ($2\theta-\omega$) or asymmetric (reciprocal space mapping, RSM) geometry were recorded by Philips X'pert-PRO Empyrean diffractometer. For XRD, measurements were performed in Bragg-Brentano reflection mode. For RSM, the diffraction along the (6 4 2) plane direction is used, which allows to gain the information about in-plane epitaxy relation along [2 -2 0] direction. The topography of the substrate and film were recorded by atomic force microscopy (AFM) using a Dimension Icon system with ScanAsyst (Bruker Dimension Icon, Billerica, MA, USA). Images were collected in tapping mode (in air) using a tip with nominal radius < 10 nm. Atomic-scale imaging was performed by cross-sectional scanning transmission electron microscopy (STEM). The sample investigated by STEM was prepared by a focused ion beam machine (FEI Helios platform) using a Ga ion beam with an accelerating voltage of first 30 kV to detach the slab, and then of 5 kV to thin it down. STEM characterization was conducted with a Hitachi HF5000 equipped with a cold field emission gun operated at 200 kV and a probe aberration corrector. High-angle annular dark-field images were acquired with a probe that formed an angle of 30 mrad and a collection angle of 60–300 mrad. EDX spectra were collected using two detectors from Oxford Instruments and color-coded elemental maps were obtained using the AZtec software. Magnetization measurements were performed by Quantum Design SQUID magnetometer. All electron transport measurements were performed in a home-built set-up.

AHE, SMR, SOTs and magnetization switching measurements: To perform the electron transport experiments, 5- μm wide and 50- μm long symmetric Hall-crosses were patterned using photolithography and Ar-ion milling. For Kerr imaging, the devices were patterned in 10- μm wide and 100- μm long Hall crosses with Au contact pads. The anomalous Hall effect and spin Hall magnetoresistance measurements were carried out using a constant dc source (Keithley 6221) and a nanovoltmeter (Keithley 2182A). For current-induced switching measurements, current pulses with a duration of 100 μs were generated by a Keithley 6221 and injected into the Hall bar. After each pulse, a small excitation ($100 \mu\text{A} = 3 \times 10^9 \text{ A/m}^2$) current was applied to evaluate and measure the magnetization state. For the harmonic Hall

measurements, an ac current source with an amplitude from 1 to 6 mA (root mean square) was injected with a Keithley 6221 current source. The first and second harmonic signals were measured using an SR-830 lock-in amplifier.

DMI measurements: The Dzyaloshisnii-Moriya interaction energy was measured by Brillouin light scattering (BLS) using a JRS TFP-2 triple-pass tandem Fabry-Perot interferometer with quarter-wave antireflection optics and linearly polarized (10 mW laser with 473 nm wavelength). The spectra were recorded in the backscattering geometry at various wave vector orientations, selected by mounting the sample on an angle-controlled sample holder providing a range of 10° to 60° incident angles corresponding to wave vectors, $q_k = (4\pi/\lambda) \sin \theta$, lying in the range 4 to $20.4 \text{ rad./}\mu\text{m}^{-1}$. The free spectral range was 9.4 or 18.7 GHz and spectra were recorded with 1024 points. The in-plane magnetic field to pull the magnetization in-plane for the Damon-Eshbach geometry is provided by permanent magnets to avoid limit thermal drifts.

Micromagnetic simulations: The micromagnetic simulations were carried out by using the GPU accelerated MUMAX³ code¹. The simulations were done for 10 nm thickness and $4 \mu\text{m}$ diameter, using a grid size $1024 \times 1024 \times 1$, and cell size $5 \text{ nm} \times 5 \text{ nm} \times 10 \text{ nm}$. Micromagnetic parameters were saturation magnetization, 95 kA/m, exchange constant, $A_{\text{ex}} = 2.1 \text{ pJ/m}$, uniaxial anisotropy, $K_u = 5.87 \times 10^3 \text{ J/m}^3$, cubic anisotropy, $K_c = -0.44 \text{ kJ/m}^3$, and damping, $\alpha = 0.01$. The efficiency for DL and FL torques were used as 0.03 and 0.02, respectively. These simulations were performed in absence of external magnetic field. The temperature of the simulation was set to 300K. The above used parameters are taken from our experiments.

II. TmIG thickness dependent X-ray diffraction

The peak (4 4 4) correspond to TmIG is observed as discussed in Fig.1 (main text). XRD peak in Pt (6 nm) at grazing incident XRD, reveals the polycrystalline phase of Pt.

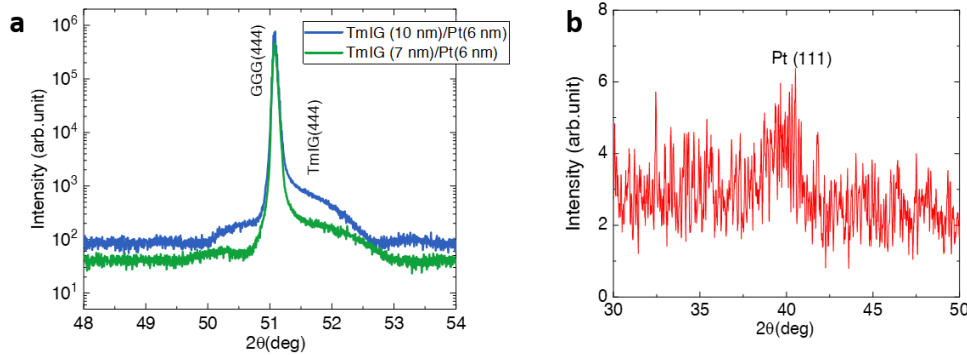


FIG. S1. **a** XRD patterns recorded on TmIG (10 nm, 7nm) with Pt(6nm). **b** Grazing incident XRD pattern around Pt (1 1 1).

III. X-ray photoelectron spectroscopy (XPS)

Total area (A) under the curve corresponds to the Tm ($A_{\text{Tm}} = 3080$ arb. units) and Fe ($A_{\text{Fe}} = 5327$ arb. units) elements are calculated using casa-XPS fitting tool. Using the relative sensitivity factor (S) of Tm ($S_{\text{Tm}} = 1.81$) and Fe ($S_{\text{Fe}} = 2.971$), the ratio of $[\text{Tm}]/[\text{Fe}]$ is evaluated through $(A_{\text{Tm}}/S_{\text{Tm}})/(A_{\text{Fe}}/S_{\text{Fe}})$ and found to be 0.57, close to the expected 0.6 for the stoichiometric sample.

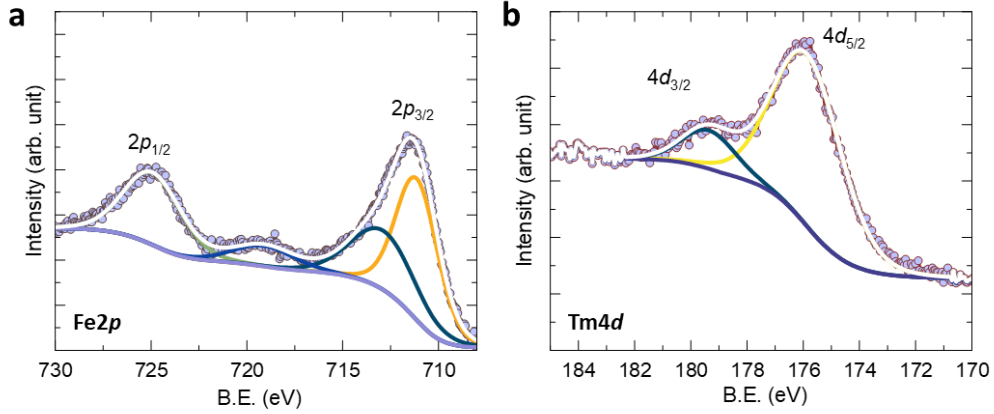


FIG. S2. In-situ XPS spectra recorded on TmIG(10 nm) thin film. Data points are the experimental results, and the lines denote the fits and the de-convoluted single peaks.

IV. SQUID out-of-plane magnetization loop, magnetization at saturation

The magnetization response of the TmIG(10 nm) was recorded using SQUID-VSM at room temperature. Magnetization hysteresis curve measured in the out-of-plane magnetic field shows in Figure S3 where the full remnance reveals the presence of PMA. The value of saturation magnetization is found to be 90 ± 10 kA/m, comparable to the TmIG bulk value².

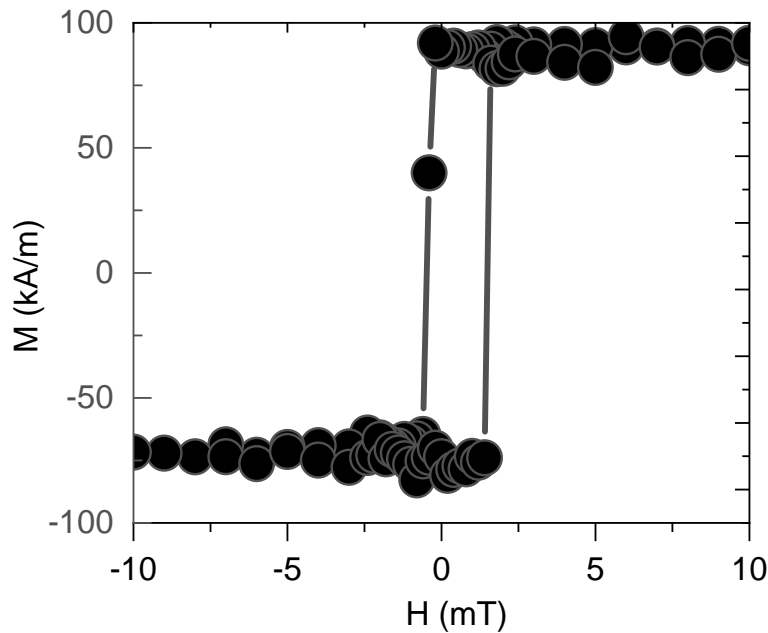


FIG. S3. SQUID magnetization hysteresis of TmIG(10 nm) film grown on GGG.

V. Resistivity

The resistivity was measured in 4 probes contact as a function of the temperature for various thicknesses of TmIG/Pt bilayers. The results are presented in Figure S4b and leads to a typical metallic resistivity for Pt(6 nm) to Pt(4 nm) in the range of $15 \mu\Omega$ cm to $25 \mu\Omega$ cm. It is clear

(from Pt(6nm) sample) that the TmIG is perfect insulator. Minute differences is expected due to the statistical error in the device and thickness measurements.

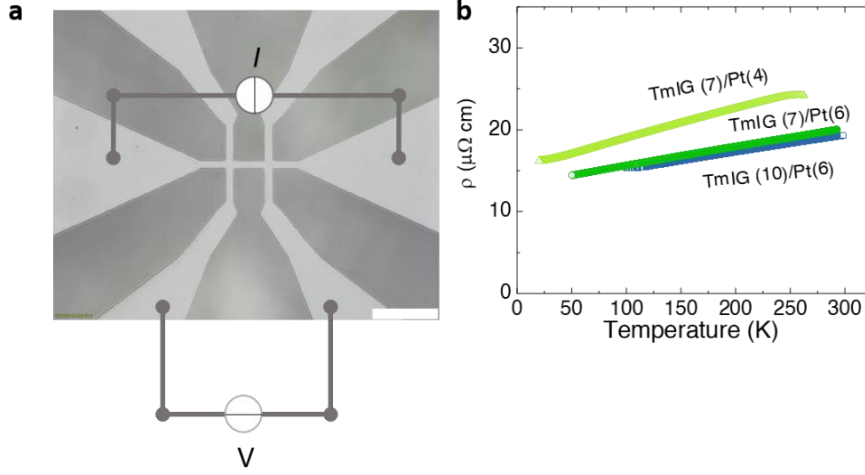


FIG. S4. **a** Device and circuit geometry for resistivity measurements; scale bar, 40μm. **b** Temperature dependent resistivity of TmIG/Pt bilayers.

VI. Spin Hall magnetoresistance (SMR) and anomalous Hall effect (AHE)

The magnetoresistance (MR) of a single metallic ferromagnetic material (FMs) depends on the angle between the current and the magnetization originating from the spin-orbit coupling and is referred as anisotropic magnetoresistance (AMR). Now considering the FIMI/HM bilayer with a current flow along the x-direction in the HM owing to the mechanism of spin Hall effect (SHE), the polarized spin (along the y-direction) (σ) interacts with the magnetization (\mathbf{M}) through the spin transfer torques. Depending on the relative angle between magnetization and the spin polarization, i.e., $\mathbf{M} \parallel \sigma$ or $\mathbf{M} \perp \sigma$, the spin-flip scattering will be minimum or maximum. This phenomenon is related to the absorption or reflection of the spin current density J_s at the FIMI/HM interface³. Accordingly, the longitudinal and transverse resistivities are governed by the magnetization components through^{3,4},

$$\rho_{xx} = \rho_0 + \Delta\rho_{\text{SMR}} m_y^2 + \Delta\rho_{\text{AMR}} m_x^2 \quad (\text{S1})$$

$$\rho_{xy} = \Delta\rho_{\text{PHE}} m_x m_y + \Delta\rho_{\text{AHE}} m_z \quad (\text{S2})$$

where m_x , m_y , and m_z are the x-component ($\propto \cos(\phi_M)$), y-component ($\propto \sin(\phi_M)$), and z-component, respectively of the magnetization at fixed magnetic field. $\Delta\rho_{\text{SMR}}$ is the change in the resistivity due to SHE/Inverse SHE, which depends on several factors such as spin mixing conductance, spin Hall angle, thickness, spin diffusion length, and conductivity of HM. In case of negligible AMR ($\Delta\rho_{\text{AMR}} \rightarrow 0$), $\Delta\rho_{\text{PHE}} = \Delta\rho_{\text{SMR}}$. The expression of SMR^{3,5} (ferromagnetic insulator as TmIG),

$$\frac{\Delta\rho_{\text{SMR}}}{\rho_0} = \theta_{\text{SHE}}^2 \frac{\lambda_s}{t_{\text{Pt}}} \frac{2G_{\uparrow\downarrow} \rho_s^{\text{Pt}} \tanh^2\left(\frac{t_{\text{Pt}}}{2\lambda_s}\right)}{1 + 2G_{\uparrow\downarrow} \rho_s^{\text{Pt}} \coth\left(\frac{t_{\text{Pt}}}{\lambda_s}\right)} \quad (\text{S3})$$

with $G_{\uparrow\downarrow}$ the spin-mixing conductance at the TmIG/Pt interface reflecting the absorption of the transverse spin-current. λ_s , and t_{Pt} are the spin diffusion length and thickness of Pt, respectively. θ_{SHE} is the spin Hall efficiency. ρ_s^{Pt} is the resistivity of Pt.

Hence, due to inverse SHE as a result of spin scattering from the surface/interface of HM, additional charge current can be generated and contributes to the measured voltage, thus concomitantly, SHE and ISHE driven MR is known as spin Hall magnetoresistance (SMR). Note that the thickness of HM should be of the order or larger than the spin diffusion length (λ_s) to develop charge-spin interconversion. In this work, we are using Pt thickness in the range of 4 to 6 nm (i.e. larger than the Pt (ref.⁶) $\lambda_s \approx 3$ nm) and a magnetic insulator (TmIG) as a ferromagnetic electrode. Magnetic insulator provides an extra degree of freedom whereas the totality of the current passes through the Pt and, hence, the change of MR purely reflects the interface phenomena. It is established that the SMR at FIM insulator interfaces is significantly large⁷ in contrast to the metallic systems⁸, due to the lack of spin-absorption in the collinear spin-magnetization configuration. Thus, due to the insulator character of the FM layer, the spin dynamics response is considerably affected. It results that SMR is an important parameter reflecting the spin mixing conductance at the interface as well as the spin Hall angle of the HM, which determines the amplitude of the effect. Moreover, it is a needed value for 2nd harmonic measurement and estimation of the torques.

The Hall- cross bar geometry (cf. Fig. S5a) is employed to investigate the electron-transport properties. A schematic model (Fig. S5b) represents the different vector components (current, magnetization, external field, SOTs) in the bilayers. The anomalous Hall effect (AHE) signal measured in the out-of-plane magnetic field geometry with an injected dc source of 300 μ A (1×10^{10} A/m²) shown in Figure S5c and a magnitude of R_{AHE} is found to be 0.55 m Ω . The observation of a sharp and square loop strongly indicates a preferred perpendicular magnetic anisotropy in TmIG/Pt. Since the ferromagnetic layer is insulating, two mechanisms could be involved in the AHE cycle: 1) the spin Hall effect (SHE) induced spin Hall magnetoresistance (SMR) and 2) a proximity effect induced AHE by which the spin-dependent scattering⁶ at the interface leading to spin current and AHE via the large SHE from Pt. Proximity effect induced AHE may also be involved but from our measurements, no AMR was observed. Its contribution is supposed to be negligible as compared to SMR. The coercivity of the AHE loop is relatively larger than the coercivities obtained using magnetic measurements (SQUID VSM), which eventually arises due to the geometrical confinement effect after patterning film.

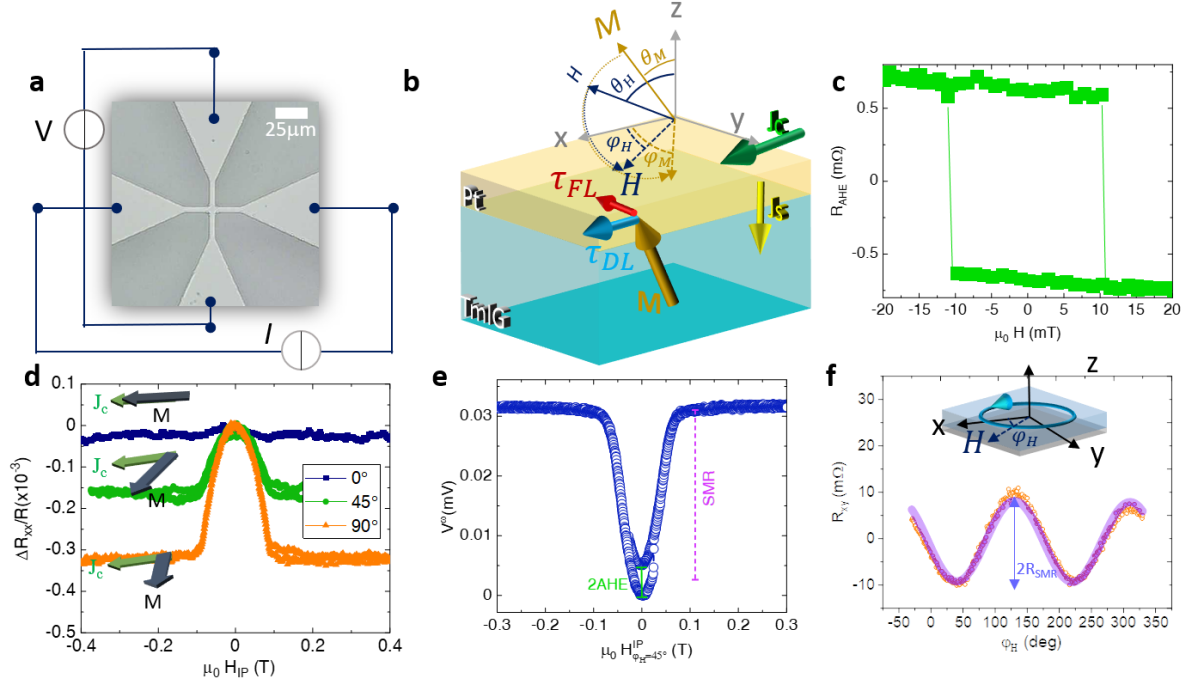


FIG. S5. **a** Symmetric Hall-cross of TmIG(10 nm)/Pt(6 nm) device for all-electron transport measurements. **b** Vector schematic model for charge current induced dynamics of magnetization. Spherical polar co-ordinates are also drawn for SMR and SOTs measurements used in later section. **c** AHE induced transverse resistance in presence out-of-plane magnetic field. **d** Longitudinal magnetoresistance under in-plane magnetic field at difference different azimuthal angles φ_H . Sketches showing the relationship between the magnetization (\mathbf{M}) and current (\mathbf{J}_c) for each rotation geometry. **e** First harmonic voltage in the in-plane magnetic field at $\varphi_H = 45^\circ$. The magnitudes corresponding to AHE and SMR are shown with the vertical arrows. **f** Angle-dependent transverse resistance (R_{xy}) in the in-plane magnetic field of 0.5T. The peak-to-peak signal is the $2 \times R_{SMR}$. The line is fit to Equation S4. The measurement geometry schematic is shown in the inset.

Now, the longitudinal resistance (R_{xx}) was measured as a function of the in-plane external magnetic field with a constant dc source (1×10^{10} A/m²) at different azimuthal angles (φ_H). As discussed above, SMR can be explained by considering the simple rule of scattering/reflection phenomena depending on the angle between the magnetization and the polarized spins (parallel or perpendicular). This can be probed by measuring the change in $R_{xx}(H, \varphi)$, i.e., $\Delta R_{xx}(H, \varphi)/R_{xx}(H, \varphi) = [R_{xx}(H, \varphi) - R_{xx}(H=0, \varphi)]/R_{xx}(H=0, \varphi)$ for different (φ_H) orientations, such as $H(\varphi = 0^\circ)$, to $H(\varphi = 90^\circ)$ as a function of in-plane magnetic field shown in Fig. S5d. It can be seen that the resistance of the TmG/Pt bilayer is respectively maximum (minimum) when the current and magnetization are respectively perpendicular (parallel) to each other, which is the signature of the SMR. Negligible AMR ($\Delta\rho_{AMR} \approx 0 \sim 0$) for $H(\varphi = 0^\circ)$ indicates that the signal observed at $H(\varphi = 90^\circ)$ is mainly due to the SMR. Further, the evidence is visible in the transverse voltage signal for an in-plane field (at $H(\varphi = 45^\circ)$), which simultaneously gives the AHE hysteresis at low field region as shown in Fig. S5e overlapped with the large SMR signal. The AHE hysteresis is shown around the zero field and the saturation of the SMR represent

the anisotropy field of the bilayer. It was predicted that an anomalous Hall-type SMR contribution stems from the significant imaginary part of the spin mixing conductance in FIMI⁹. Now, in order to estimate quantitatively the SMR contribution, angle dependent transverse resistance (R_{xy}) is measured for large in-plane magnetic field (sufficient to saturate), which follows, :

$$R_{xy} = R_0 + R_{AHE} \cos(\theta_H) + R_{SMR} \sin(\theta_H) \sin(2\phi_H), \quad (S4)$$

where R_0 is the offset (independent of magnetization), R_{SMR} , which mimic the planar Hall effect of conventional ferromagnet, is the resistance due to SMR. If H is large enough, M is parallel to H . Figures 2e S5f shows the azimuthal angle dependent R_{xy} recorded with a 0.5 T in-plane magnetic field $H(\phi, \theta = 90^\circ)$ (measurement schematic is shown in the inset). Likewise, the applied field is large enough to saturate the magnetization in plane (i.e., $\theta_H = \theta_M$). By fitting the R_{xy} vs ϕ_H using Equation S3, R_{SMR} is found to be 8.5 ± 0.1 m Ω . Now utilizing the R_{AHE} obtained from (Fig. S5c), we can define the ratio of SMR to AHE, $\epsilon_{SMR} = R_{SMR}/R_{AHE}$ equals 15.5 ± 0.2 , which is approximately one order of magnitude larger than the conventional metallic systems¹⁰. It stems from the large (real) spin-mixing conductance in FIMI/Pt. We further discussed the SMR in different sets of samples with varying TmIG and Pt thicknesses in the next section. The value of ϵ_{SMR} will be used in the SOTs calculation discussed in the forthcoming section.

VII. Spin Hall magnetoresistance in different TmIG thickness

Figure S6 shows the transverse resistance as a function of azimuthal angle $H(\phi)$ for TmIG(7nm)/Pt(6 nm), TmIG(3.6 nm)/Pt(6 nm), and TmIG(10 nm)/Pt(3 nm). With the measure of the AHE (not shown), we can extract the magnitude of $\epsilon_{SMR} = R_{PHE}/R_{AHE}$. It leads to a value of 14.1 ± 0.8 for TmIG(7 nm)/Pt(6 nm), which is smaller than the TmIG(10 nm)/Pt(6 nm) (FIG.S5e). Similarly, for TmIG(3.4 nm)/Pt(6 nm), it reduced to 8.5 ± 1.1 . Further, ϵ_{SMR} in TmIG (10 nm)/Pt(3 nm) is found to be 1.5, which is quite small as compared to other samples with thicker Pt. All values are compared in Table-I Therefore, it is clear that the thicker Pt(6 nm) is better for producing significant SHE and the subsequent SMR effects.

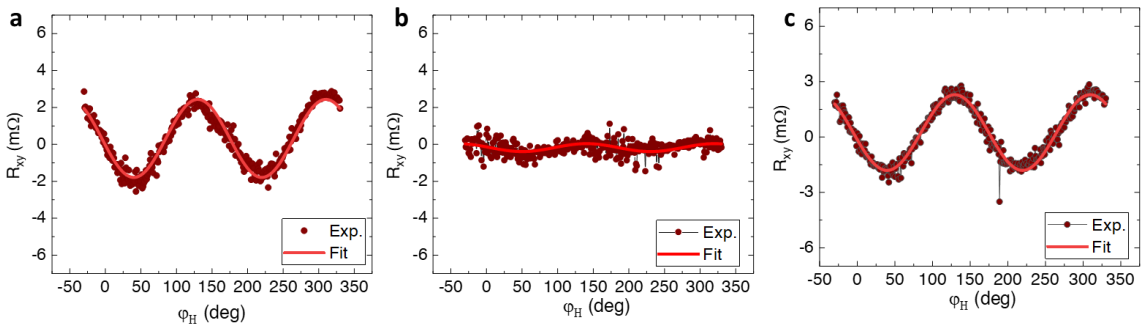


FIG. S6. **a, b, c** Transverse Resistance vs. ϕ_H for TmIG(7 nm)/Pt(6 nm), TmIG(3.6 nm)/Pt(6 nm) and TmIG(10 nm)/Pt(3 nm), respectively.

Table-I: SMR ratio for different heterostructures

Layer stack	SMR ratio (ϵ_{SMR})
TmIG(7 nm)/Pt(6 nm)	14.1±0.8
TmIG(10 nm)/Pt(6 nm)	15.5±0.2
TmIG(10 nm)/Pt(3 nm)	1.5±0.3
TmIG(3.4 nm)/Pt(6 nm)	8.5±1.1

VIII. Harmonic Hall measurements: Spin orbit torques

Adiabatic harmonic Hall voltage approach has been used to quantify the components of SOT, i.e., effective fields using a lock-in detection-based technique. In this system, one can control the magnetization orientation relative to the applied current in all xyz-orientations. The transverse Hall-voltage V_H is measured with the magnetic field in the film-plane. Since the magnetization is in the film plane, therefore, a resulting voltage V_H comprises both the anomalous Hall voltage (V_{AHE}) (due to spin-orbit fields vis-à-vis SHE) and SMR (V_{SMR}) (due to SMR)¹¹.

$$V_H = V_0 + V_{AHE} \cos(\theta_M) + V_{SMR} \sin \theta_M \sin (2\varphi_M), \quad (S5)$$

where V_0 is the voltage due to imperfect Hall-cross geometry and independent of magnetization. θ_M and φ_M are the angles depicted in Figure S5a. Note that Equation (S5) is like Equation (S4) except that the angle refers now to account for the magnetization direction and not the magnetic field. When using an AC, $I(t) = I_0 \sin(\omega t)$ with an amplitude I_0 and a low frequency, $\omega/2\pi = 441$ Hz (in our experiments), the signal can be decomposed, respectively as $V^{1\omega}$ (first harmonic) and $V^{2\omega}$ (second harmonic) voltages. The latter arises due to the mixing of the AC with the oscillations of the magnetization induced by SOTs around its equilibrium position, which change $\theta_M \rightarrow \theta_M + \Delta\theta_M$ and $\varphi_M \rightarrow \varphi_M + \Delta\varphi_M$. As a result,

$$V_H = V_0 + V^{1\omega} \sin(\omega t) + V^{2\omega} \sin(2\omega t), \quad (S6)$$

where,

$$V^{1\omega} = V_0 + V_{AHE} \cos(\theta_M) + V_{SMR} \sin \theta_M \sin (2\varphi_M), \quad (S7)$$

and

$$V^{2\omega} = \frac{1}{2} [V_{AHE} \sin(\theta_M) - V_{PHE} \sin (2\theta_M) \sin (2\varphi_M)] \Delta\theta_M - V_{SMR} \sin^2 \theta_M \cos (2\varphi_M) \Delta\varphi_M, \quad (S8)$$

where (θ_M, φ_M) are the equilibrium positions and $(\Delta\theta_M, \Delta\varphi_M)$ are magnitude of oscillations or perturbations of the magnetization due to effective magnetic fields generated by SOTs. Note that magnetization oscillation also depends on the external field H_{ext} , and the anisotropy field H_k . Since, the magnetization oscillation amplitudes $\Delta\theta_M$ and $\Delta\varphi_M$ depend on the current induced SOTs, the equivalent magnetic field resulting from torque (H_{DL} and H_{FL}) can be extracted from the following analytical expressions¹¹,

$$\Delta\theta_M = \frac{H_{DL} \cos\varphi_M + H_{FL} \cos\varphi_M \sin\varphi_M}{H_k \cos(2\theta_M) + H_{ext} \cos(\theta_M - \theta_H)}, \quad (S9)$$

and

$$\Delta\varphi_M = \frac{-H_{DL} \cos\varphi_M \sin\theta_H - \Delta H_x \cos\varphi_M}{H_{ext} \sin(\theta_H)}, \quad (S10)$$

where H_{DL} , and H_{FL} , are the respective spin orbit fields due to the damping-like and field-like torques, respectively. Now, in a perpendicular magnetic system when the magnetic field is applied in the plane of the sample parallel (longitudinal configuration) or perpendicular (transverse configuration) to the current, i.e., x-axis ($\varphi_M = 0^\circ$ or $\varphi_H = 90^\circ$) and $\theta_H = 90^\circ \pm \delta\theta_H$ ($\delta\theta_H$; a little tilt from the x-y plane to avoid multi domain state), using Equations S7, S8 and S9, the second harmonic voltages corresponding to longitudinal ($V_L^{2\omega}$) and transverse configuration ($V_T^{2\omega}$) can be expressed as¹¹,

$$V_L^{2\omega} = \frac{V_{AHE}}{2} \left[\frac{\sin\theta_M}{H_K^{eff} \cos 2\theta_M + H \cos(\theta_M - \theta_H)} H_{DL} - \frac{\epsilon_{SMR} \sin 2\theta_M}{H \sin\theta_H} H_{FL} \right], \quad (S11)$$

$$V_T^{2\omega} = -\frac{V_{AHE} \cos(\theta_M)}{2} \left[-\frac{\sin\theta_M}{H_K^{eff} \cos 2\theta_M + H \cos(\theta_M - \theta_H)} H_{FL} + \frac{\epsilon_{SMR} \sin 2\theta_M}{H \sin\theta_H} H_{DL} \right], \quad (S12)$$

where ϵ_{SMR} is the ratio between SMR and AHE, as previously discussed. One can note that depending on the value of the ϵ_{SMR} ratio the mixing of the contribution of the H_{DL} and H_{FL} in the longitudinal and transverse geometry can be more or less important. In metallic systems the ratio is generally small, and the longitudinal geometry is more sensitive to H_{DL} whereas transverse geometry is more sensitive to H_{FL} . It is important to notice that we are not in this limit, $\epsilon_{SMR} \gg 1$ and involves both term in the two geometry and eventually makes that H_{DL} dominate in the transverse geometry whereas H_{FL} dominate in the longitudinal geometry.

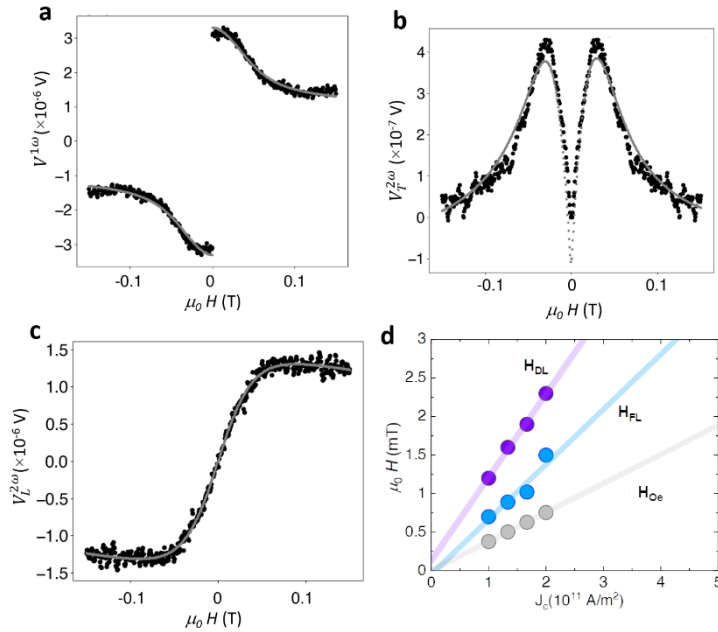


FIG. S7. **a** First harmonic voltage ($V^{1\omega}$) in the in-plane applied field. Line is fit to the Equation S13. Second harmonic signals correspond to **b** FL and **c** DL geometry, respectively for $J_c \perp H_{ext}$ and $J_c \parallel H_{ext}$. Lines are fit to the Equation S12 and S11 for FL and DL curves, respectively. **d** H_{DL} and H_{FL} values as a function of current density in the Pt layer. Lines are the linear fit. The values of H_{Oe} at all J_c are evaluated by considering the Pt thickness and the width of the device.

Before calculating H_{DL} and H_{FL} , we estimate H_k , $\delta\theta_H$ and θ_M using first Harmonic signal (shown in Figure S7a) through $\cos(\theta_M) = V^{1\omega}/V_{AHE}$, where V_{AHE} is the anomalous Hall voltage (c.f Figure S5c). Let's first understand the variation of θ_M ; the magnetization angle varies with H_{ext} . Thus, the inclusion of θ_M in Equations S11 and S12 at all points of H_{ext} endorse the reliability of the DL/FL torques. Now to estimate these parameters, the Stoner-Wohlfarth model¹² has been used to fit the $V^{1\omega}$, which is expressed as,

$$\cos(\theta_M) = \frac{p}{6} \pm \frac{1}{6} \left[2p^2 - 18g + \frac{54H_z(1+H_x^2)}{p} \right]^{1/2} - \frac{H_z}{2}, \quad (S13)$$

where $H_x = (H_{ext}/H_k) \sin(\theta_H)$ is the in-plane component of the field, $H_z = (H_{ext}/H_k) \cos(\theta_H)$ is the out-of-plane component, $g = d \cos\left(\frac{1}{3} \cos^{-1}(54H_x^2 \frac{H_z^2}{d^3} - 1)\right)$, and $p = \pm(9H_z^2 + 6d + 6g)^{1/2}$, where $d = 1 - \left(\frac{H_{ext}}{H_k}\right)^2$. First harmonic voltage $V^{1\omega}$ together with the fitting of Equation S13 shown in Figure S7a. The H_k and $\delta\theta_H$ values are found to be 44 mT and 11°, respectively. These values are then substituted into Equations S11 and S12 and self-consistently fitted to $V^{2\omega}$ data to estimate the H_{FL} and H_{DL} as shown in Figures S7b and S7c, respectively.

The two curves are oppositely symmetric with respect to external field and current geometry. It is because the field-like torque does not vary with the magnetization direction whereas damping-like torque does. For brevity, $V_L^{2\omega}$ and $V_T^{2\omega}$ curves are shown for a 6-mA injected current. Moreover, the Anomalous Nernst effect (ANE) $\propto \sin(\theta_M)$ is also added in the fitting model, which is caused by the unintentional out-of-plane temperature gradient ΔT produced by the Joule heating and asymmetric heat dissipation that contributes to the second harmonic voltage. The magnitude of ANE voltage is found to be $\sim 0.012 \mu V$, which is relatively smaller than the SOT signals. The fitted values of SOTs fields are shown in Figure S7d along with Ørsted field generated due to the applied current calculated by Ampere's law ($H_{Oe} = J_c \times t_{Pt}/2$), which drives the magnetization to oscillate in the in-plane along the y-direction. The field due to the damping-like SOT is relatively larger than the field-like SOT, which is different from the reported values¹³ in TmIG/Pt where both SOT fields were assumed to be identical. The ratio of the H_{FL}/H_{DL} is found to be ~ 0.6 . Now we calculate the spin-torque efficiencies for the damping and field-like torques using¹⁴,

$$\theta_{SHE}^{DL(FL)} = \frac{2e}{\hbar} \frac{H_{DL(FL)}}{J_c} M_s t, \quad (S14)$$

where M_s , t , e and \hbar are the saturation magnetization, thickness of TmIG, electronic charge and reduced Planck's constant, respectively. Using the slopes of H_{DL}/H_{FL} vs. J_c from Fig. S7d into the Equation S14, the effective spin Hall efficiencies are estimated to be 0.03 ± 0.01 and 0.02 ± 0.002 , respectively for the damping and field-like torques, which is comparable to the case of YIG/Pt¹⁵.

IX. Dzyaloshinskii-Moriya Interaction (DMI) using Brillouin Light Scattering

The Brillouin light scattering (BLS) technique in the backscattering configuration and performed at controlled room temperature has been employed to determine both the symmetric exchange stiffness (A_{ex}), and the antisymmetric Dzyaloshinskii-Moriya interaction

(DMI) strength in TmIG/Pt bilayers. In this measurement, the propagating spin waves are being probed in thin film of FIMI where the DMI manifests as a non-reciprocity for the spin waves. Thus, for a given wavelength, the two spin waves propagating in opposite directions have different frequencies while the magnetization lies in the film-plane and for the wave vector is perpendicular to it. The magnetic field was applied perpendicular to the incidence plane, allowing spin waves propagating along the in-plane direction perpendicular to the applied field to be probed, the so-called Damon-Eshbach (DE) geometry. The frequency (f) vs. wave vector (k) dispersion was measured using oppositely propagating spin waves in TmIG. The BLS spectra were obtained at several incident angles (θ) (i.e., wave vectors $q = (4\pi/\lambda) \sin \theta$, which were then fitted with a Lorentzian function to determine the Stokes (S , negative frequency shift related to the incident light as the SW was created) and anti-Stokes (AS , the positive frequency shift related to the incident light where the SW was absorbed) frequencies. The fit provides peak frequency and width for both anti-Stokes and Stokes conditions. Here λ is the wavelength (473 nm) of the blue laser. BLS spectra measured on TmIG(15 nm)/Pt(6 nm) at various wave vectors (Figure 2, main text), fitted with the Lorentzian function. The frequency correspond to anti-Stokes (f_{AS}) are plotted against the wave vector (q) shown in Fig.S8c to estimate the exchange constant by using a Kittel Equation¹⁶,

$$f_{AS} = \frac{\gamma\mu_0}{2\pi} \left[\left(H + \frac{2A_{ex}}{\mu_0 M_s} q^2 + \eta(qt)M_s \right) \left(H + \frac{2A_{ex}}{\mu_0 M_s} q^2 + \eta(qt)M_s + H_{keff} \right) \right]^{\frac{1}{2}} - \frac{\gamma}{\mu_0 M_s} qD, \quad (S15)$$

$$\eta(qt) = 1 - \frac{1 - e^{-|q|t}}{|q|t}, \quad (S16)$$

where γ is the gyromagnetic ratio, μ_0 is the magnetic permeability of vacuum, H is applied in-plane magnetic field. The term η accounts for the influence of dipolar interactions on the spin waves. $H_{keff} (=H_k - M_s)$ is the effective anisotropy field and H_k is the perpendicular anisotropy field. Using the obtained parameters and fitting of Equation S16 to the f_{AS} vs. q curves, the value of A_{ex} is found to be 2.1 ± 0.05 pJ/m. Now, to estimate the value of DMI, the difference in the Stokes anti-Stokes frequencies ($\Delta f = f_{AS} - f_S$), originating from the spin-waves with opposite ($+q$ and $-q$) wave-vectors, is considered. The frequency difference is related to DMI is as follows,

$$\Delta f = f(q+) - f(q-) = \frac{2\gamma q D}{\pi M_s}, \quad (S17)$$

where Δf is the frequency difference, γ is the gyromagnetic ratio, D is the DMI constant, M_s is the magnetization saturation. The results for TmIG15nm//Pt6nm is presented in the main text (Figure 2). We also estimated the DMI for several TmIG thicknesses as shown in Figure S9. The linear change of D with inverse of the thickness reveals the non-reciprocity appears right at the TmIG/Pt interface. However, finite intercept shows suggest bulk DMI contribution of TmIG, which is undetectable in BLS (Figure 2e).

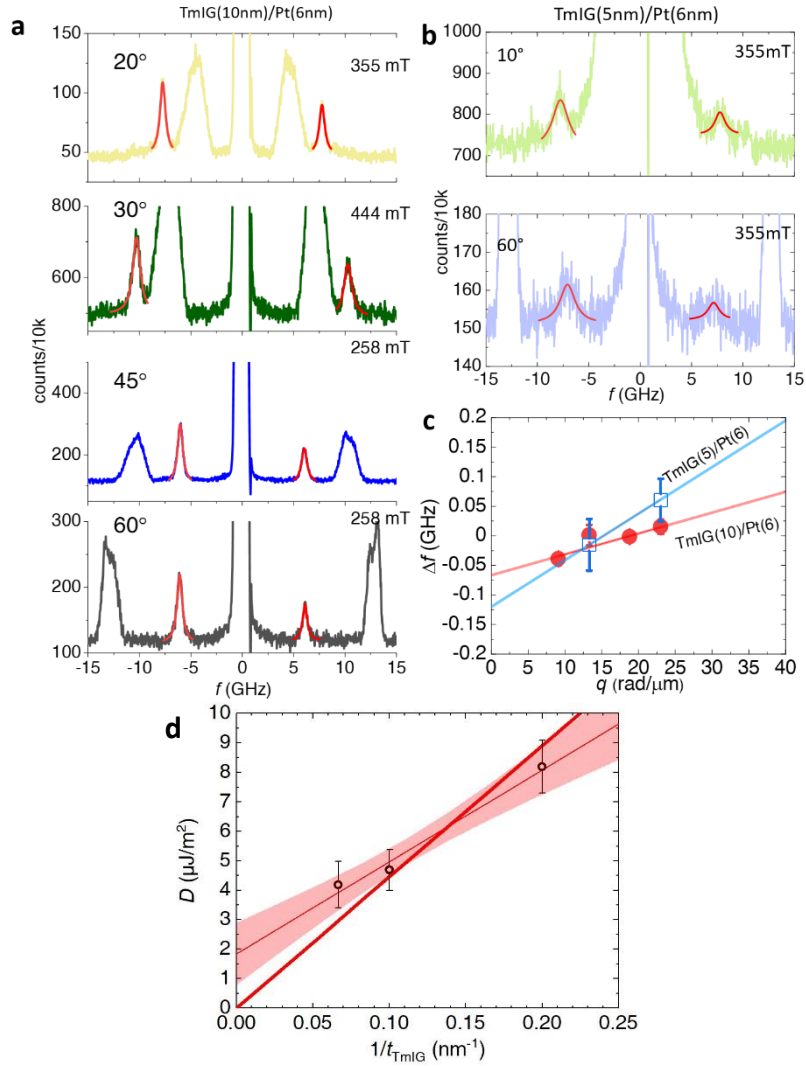


FIG. S9. **a, b** Measured spectra at different angles (θ) at constant in-plane magnetic fields for two samples of different TmIG thickness. Different magnetic fields were chosen to avoid the phonon spectrum overlapping. Symbols represent experimental data and lines are fit to the Lorentzian function. **c** Frequency difference Δf vs. q . Line is fit to the DMI Equation (S16). **d** DMI vs. inverse of the TmIG thickness. Shaded line is fit the 10% confidence interval. Solid line is forced linear fit through zero, which is an indicative of the small contribution from the bulk TmIG.

X. Switching in TmIG(10)/Pt(6) in residual magnetic field (including earth magnetic field) only
 In the following we present some experiments performed with the aim to rule out any possible in plane residual magnetic field during the experiment which has been discussed in the main text. Current reversal recorded at different θ_H angles (defined one more time in Fig. S10a) in the cryostat without applying any field is shown in Figure S10. If a residual in plane magnetic field subsists the θ_H rotation should change this contribution as $H \cdot \sin(\theta_H)$. From the results, the magnetization reversal at zero magnetic field is not affected. It confirms that the observed magnetization switching is free from any external magnetic field contributions. As a final test the device was removed from the cryostat and the magnet and

still magnetization reversal was observed as shown in Fig. S10c. A stochastic behaviour was also recorded at very high current density, which may occur due to the domain wall reflection¹⁷.

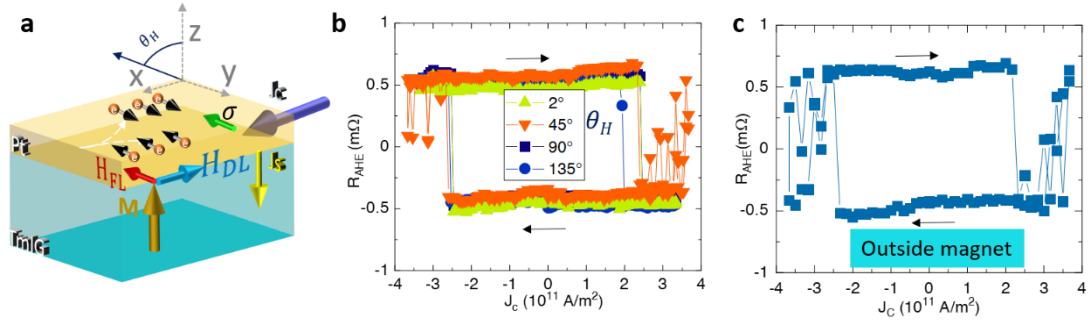


FIG. S10. **a** Vector schematic of current induced SOTs, magnetization, and field. **b** Current reversals at different rotation angles θ_H from out-of-plane to in-plane rotation (zero-field withing magnetic poles). **c** Magnetization switching curve recorded outside the magnet (in earth magnetic field only). All magnetization reversals were recorded in absence of applied magnetic field.

XI. Zero-field switching in TmIG(7 nm)/Pt(6 nm) and TmIG(10 nm)/Pt(4 nm) bilayer devices

We performed the same measurements as shown in Figure 2(main text) for the for varying TmIG and Pt thickness devices. Here we also observed the switching without magnetic field in lower thickness of TmIG shown in Figure S11a. The AHE and current induced switching measured in TmIG(10)/Pt(4) shows in Figure S11b. The signal strength is larger than the AHE measured with Pt(6), which is expected as the AHE scale with the Pt resistance, i.e., $R_{AHE} \propto R_{Pt}^2$ (ref.¹⁸). The resistivity data is shown in section V. We also note that the critical current density of magnetization switching is smaller with thinner Pt thickness. The current induced switching is measured in absence of the magnetic field.

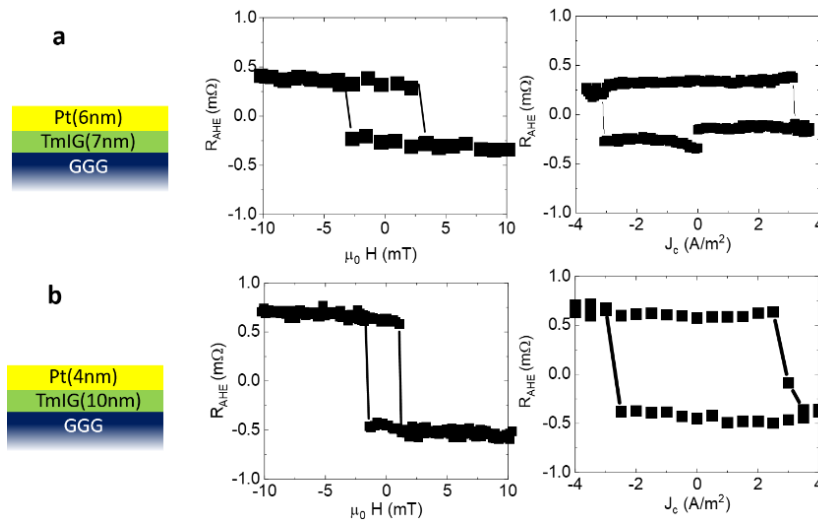


FIG. S11. Anomalous Hall effect and switching in **a** TmIG(7 nm)/Pt(6 nm), **b** TmIG(10 nm)/Pt(4 nm)

XII. Magnetization switching map in different devices of TmIG(10 nm)/Pt(6 nm)

In order to fully characterize the magnetization reversal process, we have also recorded the influence of a magnetic field, as reported in Fig.S12. In zero field, starting from an initial state with magnetization up ($R_{\text{AHE}} < 0$, point A in Fig.3b), the system switches from up to down (blue to red) at a negative current of about ~ 7 mA ($\sim 2.5 \cdot 10^{11}$ A/m² in Fig.3b). The application of a positive field $\mu_0 H_x$ helps to switch and the switching current decreases in absolute value down to about -6 mA at ~ 10 mT. In contrast, a negative field appears to hinder the switching by a negative current and suppresses it above about -0.9 mT. For positive fields, the switching from up to down (blue to red) occurs in positive currents, which correspond to a change of the polarity of the loops, from the CW type of Fig.3b to the CCW if Fig.3c. The decrease of the switching current as the field increases expresses that negative fields help the switching of this polarity. Hence, depending on the initial state of magnetization, up/down switching is possible by using the current pulse in CW/CCW manner. This is identical to the procedure applied to the field-free magnetization switching in other systems where the initial state is set-up by the external magnetic field (Zheng et al., 2021). We thus find that, in addition to the results obtained at zero field, an applied field can help or hinder the switching and even change the polarity of the loops [27].

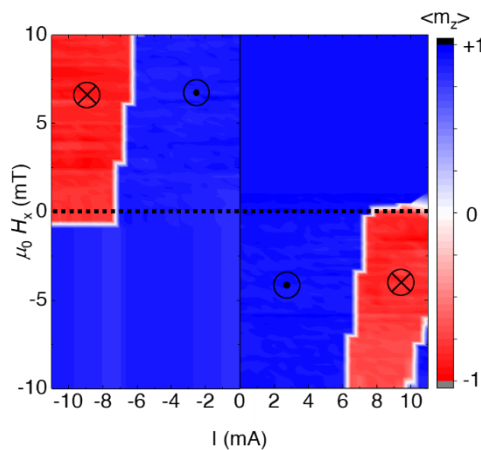


FIG. S12. **Current-field map of magnetization switching.** Experimental magnetization switching map recorded in the in-plane magnetic fields (along or opposite to the current direction) after initializing the magnetization with $+0.35$ T magnetic field. A dotted line is drawn at zero-field crossover. Scheme of the measurement: The data has been recorded only for one quadrant in each current directions with initialization in high field before each measurement. For clarity of the dotted line high current value having the same switching: For each quadrant measurements, for each data point, sample must be reset with the high magnetic field. Thus, the depending on the initial current direction, the hysteresis polarity is either clockwise or counterclockwise as shown in Figure 3 (main text).

We also observed, depending on the Hall bar as presented in Fig.S13, some asymmetry in the switching current polarity we relate to extrinsic mechanisms linked to the nucleation process (defect, shape, inhomogeneity etc.). Despite the asymmetry in the switching characteristics, a zero-field switching is inevitable. A perfect control of the shape and the edges of the ferromagnetic insulator will be needed to go behind our main result.

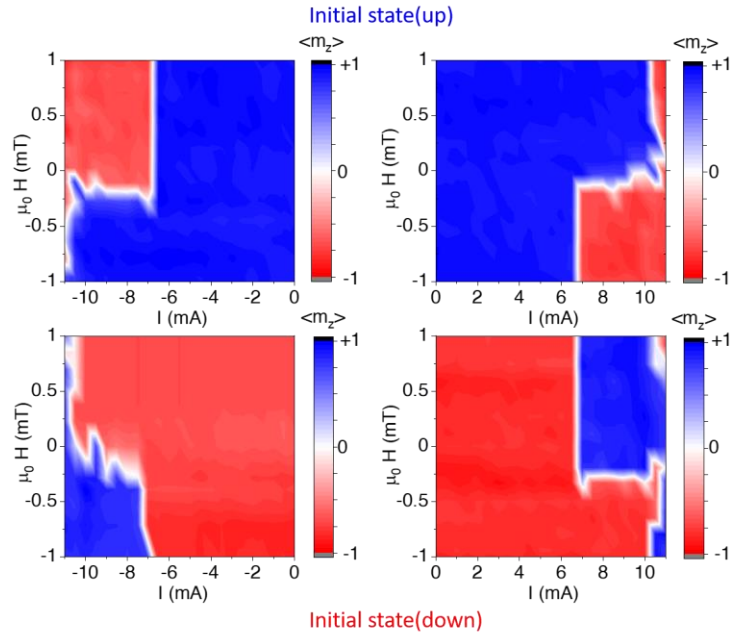


FIG. S13. Experimental magnetization switching map recorded in the in-plane magnetic fields (along or opposite to the current direction) after initializing the magnetization in two opposite configurations using 0.35T magnetic field. In each initial state (up or down), 0 to -I and 0 to +I current sweeps were done separately for range of in-plane applied magnetic fields.

XIII Kerr switching in 6-contact geometry device.

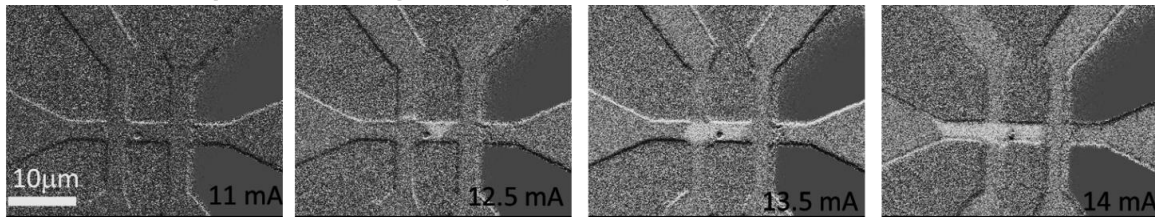


Figure S14 Kerr microscopy imaging on the TmIG(10nm)/Pt(6nm). Current direction is from the left-to-right. Due to the complex device geometry, the domain collection is a bit random. It is obvious to have random nucleation event due to the large variation of the current density in wide cross-tracks.

XV Magnetization switching in devices patterned at different angles.

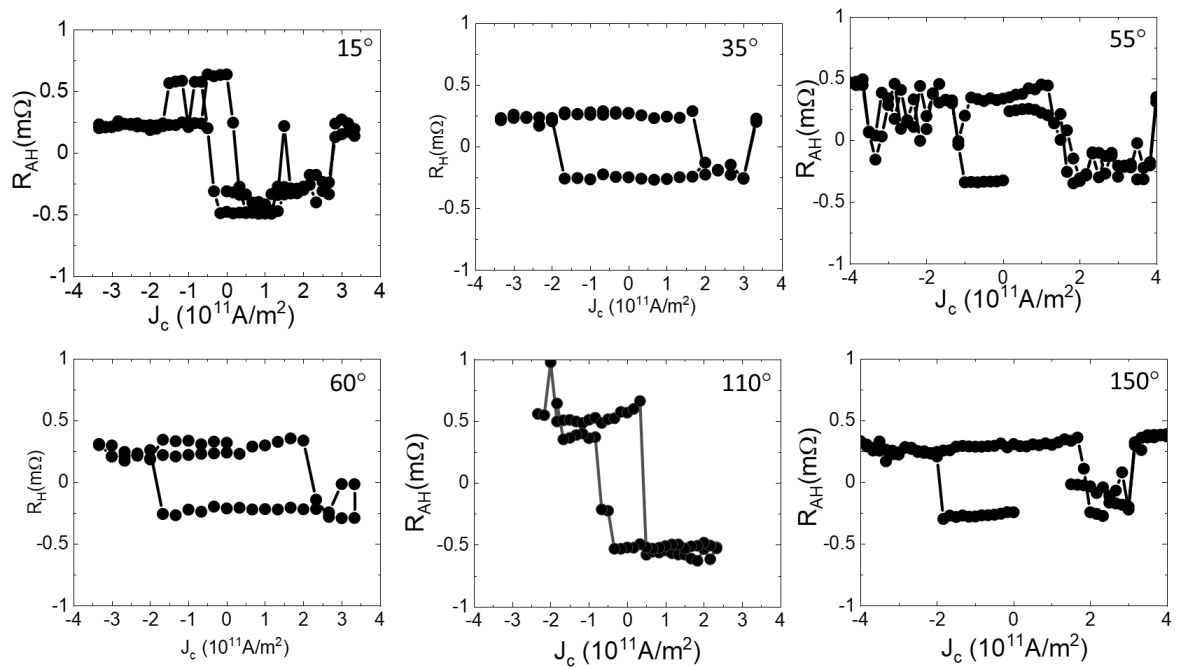


Figure S15 Field-free magnetization switching at different in-plane angled devices correspond to Figure 5 main text.

References:

- (1) Vansteenkiste, A.; Leliaert, J.; Dvornik, M.; Helsen, M.; Garcia-Sanchez, F.; Van Waeyenberge, B. The Design and Verification of MuMax3. *AIP Advances* **2014**, *4*, 107133. <https://doi.org/10.1063/1.4899186>.
- (2) Geller, S.; Remeika, J. P.; Sherwood, R. C.; Williams, H. J.; Espinosa, G. P. Magnetic Study of the Heavier Rare-Earth Iron Garnets. *Phys.Rev.* **1965**, *137* (200), 1034–1038.
- (3) Chen, Y. T.; Takahashi, S.; Nakayama, H.; Althammer, M.; Goennenwein, S. T. B.; Saitoh, E.; Bauer, G. E. W. Theory of Spin Hall Magnetoresistance. *Physical Review B - Condensed Matter and Materials Physics* **2013**, *87* (14), 144411. <https://doi.org/10.1103/PhysRevB.87.144411>.
- (4) Nakayama, H.; Althammer, M.; Chen, Y. T.; Uchida, K.; Kajiwara, Y.; Kikuchi, D.; Ohtani, T.; Geprägs, S.; Opel, M.; Takahashi, S.; Gross, R.; Bauer, G. E. W.; Goennenwein, S. T. B.; Saitoh, E. Spin Hall Magnetoresistance Induced by a Nonequilibrium Proximity Effect. *Physical Review Letters* **2013**, *110* (20), 206601. <https://doi.org/10.1103/PhysRevLett.110.206601>.
- (5) Jia, X.; Liu, K.; Xia, K.; Bauer, G. E. W. Spin Transfer Torque on Magnetic Insulators. *EPL* **2011**, *96* (1), 17005. <https://doi.org/10.1209/0295-5075/96/17005>.
- (6) Dang, T. H.; Barbedienne, Q.; To, D. Q.; Rongione, E.; Reyren, N.; Godel, F.; Collin, S.; George, J. M.; Jaffrès, H. Anomalous Hall Effect in 3d/5d Multilayers Mediated by Interface Scattering and Nonlocal Spin Conductivity. *Phys Rev B* **2020**, *102* (14), 144405. <https://doi.org/10.1103/PhysRevB.102.144405>.
- (7) Huang, S. Y.; Fan, X.; Qu, D.; Chen, Y. P.; Wang, W. G.; Wu, J.; Chen, T. Y.; Xiao, J. Q.; Chien, C. L. Transport Magnetic Proximity Effects in Platinum. *Physical Review Letters* **2012**, *109* (10), 107204. <https://doi.org/10.1103/PhysRevLett.109.107204>.
- (8) Kawaguchi, M.; Towa, D.; Lau, Y.; Takahashi, S.; Hayashi, M.; Kawaguchi, M.; Towa, D.; Lau, Y.; Takahashi, S. Anomalous Spin Hall Magnetoresistance in Pt / Co Bilayers. *Appl. Phys. Lett.* **2018**, *112*, 202405. <https://doi.org/10.1063/1.5021510>.
- (9) Weiler, M.; Althammer, M.; Schreier, M.; Lotze, J.; Pernpeintner, M.; Meyer, S.; Huebl, H.; Gross, R.; Kamra, A.; Xiao, J.; Chen, Y.; Jiao, H.; Bauer, G. E. W.; Goennenwein, S. T. B. Experimental Test of the Spin Mixing Interface Conductivity Concept. *Physical Review Letters* **2013**, *111* (October), 176601. <https://doi.org/10.1103/PhysRevLett.111.176601>.
- (10) Avci, C. O.; Garello, K.; Ghosh, A.; Gabureac, M.; Alvarado, S. F.; Gambardella, P. Unidirectional Spin Hall Magnetoresistance in Ferromagnet/Normal Metal Bilayers. *Nature Physics* **2015**, *11* (7), 570–575. <https://doi.org/10.1038/nphys3356>.
- (11) Yun, S. J.; Park, E.; Lee, K.; Lim, S. H. Accurate Analysis of Harmonic Hall Voltage Measurement for Spin – Orbit Torques. *NPG Asia Materials* **2017**, *9* (March), e449. <https://doi.org/10.1038/am.2017.200>.

- (12) Wood, R. Exact Solution for a Stoner – Wohlfarth Particle in an Applied Field and a New Approximation for the Energy Barrier. *IEEE Transactions on Magnetics* **2009**, *45* (1), 100–103.
- (13) Avci, C. O.; Quindeau, A.; Pai, C. F.; Mann, M.; Caretta, L.; Tang, A. S.; Onbasli, M. C.; Ross, C. A.; Beach, G. S. D. Current-Induced Switching in a Magnetic Insulator. *Nature Materials* **2017**, *16* (3), 309–314. <https://doi.org/10.1038/nmat4812>.
- (14) Liu, L.; Lee, O. J.; Gudmundsen, T. J.; Ralph, D. C.; Buhrman, R. A. Current-Induced Switching of Perpendicularly Magnetized Magnetic Layers Using Spin Torque from the Spin Hall Effect. *Physical Review Letters* **2012**, *109* (9), 096602. <https://doi.org/10.1103/PhysRevLett.109.096602>.
- (15) Yang, W. L.; Wei, J. W.; Wan, C. H.; Xing, Y. W.; Yan, Z. R.; Wang, X.; Fang, C.; Guo, C. Y.; Yu, G. Q.; Han, X. F. Determining Spin-Torque Efficiency in Ferromagnetic Metals via Spin-Torque Ferromagnetic Resonance. *Physical Review B* **2020**, *101* (6), 064412. <https://doi.org/10.1103/PhysRevB.101.064412>.
- (16) Belmeguenai, M.; Adam, J.; Roussign, Y.; Eimer, S.; Devolder, T.; Kim, J.; Cherif, S. M.; Stashkevich, A. Interfacial Dzyaloshinskii-Moriya Interaction in Perpendicularly Magnetized Pt / Co / AlO_x Ultrathin Films Measured by Brillouin Light Spectroscopy. *Physical Review B* **2015**, *180405*, 180405(R). <https://doi.org/10.1103/PhysRevB.91.180405>.
- (17) Yoon, J.; Lee, S. W.; Kwon, J. H.; Lee, J. M.; Son, J.; Qiu, X.; Lee, K. J.; Yang, H. Anomalous Spin-Orbit Torque Switching Due to Field-like Torque-Assisted Domain Wall Reflection. *Science Advances* **2017**, *3* (4), e1603099. <https://doi.org/10.1126/sciadv.1603099>.
- (18) Tang, C.; Sellappan, P.; Liu, Y.; Xu, Y.; Garay, J. E.; Shi, J. Anomalous Hall Hysteresis in Tm₃Fe₅O₁₂ / Pt with Strain-Induced Perpendicular Magnetic Anisotropy. *Physical Review B* **2016**, *94*, 140403(R). <https://doi.org/10.1103/PhysRevB.94.140403>.
- (19) Zheng, Z.; Zhang, Y.; Lopez-Dominguez, V.; Sánchez-Tejerina, L.; Shi, J.; Feng, X.; Chen, L.; Wang, Z.; Zhang, Z.; Zhang, K.; Hong, B.; Xu, Y.; Zhang, Y.; Carpentieri, M.; Fert, A.; Finocchio, G.; Zhao, W.; Khalili Amiri, P. Field-Free Spin-Orbit Torque-Induced Switching of Perpendicular Magnetization in a Ferrimagnetic Layer with a Vertical Composition Gradient. *Nat Commun* **2021**, *12* (1), 4522. <https://doi.org/10.1038/s41467-021-24854-7>.